Journal of Molecular Catalysis A: Chemical 390 (2014) 133–141

Contents lists available at ScienceDirect

Journal of Molecular Catalysis A: Chemical

journal homepage: www.elsevier.com/locate/molcata

Sol–gel synthesis and photocatalytic activity of ZnO–SnO_2 nanocomposites

Abdessalem Hamrouni[a,b], Noomen Moussa[a], Francesco Parrino[b], Agatino Di Paola[b,*], Ammar Houas[a,c], Leonardo Palmisano[b]

[a] Unité de Recherche Catalyse et Matériaux pour l'Environnement et les Procédés URCMEP (UR11ES85), Faculté des Sciences de Gabès/Université de Gabès, Campus Universitaire, Cité Erriadh, 6072 Gabès, Tunisie
[b] Dipartimento di Energia, Ingegneria dell'Informazione e Modelli Matematici (DEIM), University of Palermo, Viale delle Scienze Ed. 6, Palermo 90128, Italy
[c] Al Imam Mohammad Ibn Saud Islamic University (IMSIU), College of Sciences, Department of Chemistry, Riyadh 11623, Saudi Arabia

ARTICLE INFO

Article history:
Received 12 November 2013
Received in revised form 6 March 2014
Accepted 8 March 2014
Available online 5 April 2014

Keywords:
Photocatalysis
ZnO–SnO_2 nanocomposites
Sol–gel method
Heterojunction effect

ABSTRACT

ZnO–SnO_2 nanocomposites were synthesized by a facile sol–gel synthesis route and characterized through X-ray diffraction, BET specific surface area analysis, UV–vis diffuse reflectance spectroscopy, photoluminescence spectroscopy, X-ray photoelectron spectroscopy, scanning electron microscopy, transmission electron microscopy. The photocatalytic activity of the samples was tested using the degradation of 4-nitrophenol under UV light as model reaction. The ZnO/SnO_2 molar ratio was varied in order to study its influence on the photoefficiency of the samples. The ZnO–SnO_2 nanocomposites showed higher photoactivity than the pure oxides and in particular the sample with ZnO/SnO_2 molar ratio equal to 1/0.05 resulted the best one among the tested powders. The high activity of the mixed samples was attributed to the presence of heterojunctions between the two oxides, which allows an improved charge separation of the photogenerated electron–hole pairs, due to the differences between the energy levels of the conduction and valence bands of ZnO and SnO_2. Photovoltage measurements were performed to determine the energy band structure of the ZnO–SnO_2 heterojunction.

1. Introduction

Since Fujishima and Honda in 1972 [1] described the photoelectrolysis of water using supported TiO_2 as photoanode, heterogeneous photocatalysis has been object of considerable attention in the field of green chemistry and of "Advanced oxidation processes" (AOPs) [2–4] mainly for air and water remediation [5].

When a photocatalyst is irradiated with light of energy equal or higher than its band gap energy, electron/hole pairs (e^-/h^+) are produced. In an aqueous or gaseous medium, reactants can adsorb on the photocatalyst surface and react directly or indirectly with the photogenerated electrons and holes.

ZnO is a semiconductor material with band gap energy of 3.2 eV, thus absorbing in the UV region of the electromagnetic spectrum [6]. ZnO has been broadly studied as a photocatalyst due to its low cost, and its good optoelectronic and catalytic properties [5]. In several reports, ZnO was found efficient for the photodegradation of many non-biodegradable organic compounds [7–14] due to the position of its valence band which gives a strong oxidizing power to the photogenerated holes [7]. However, the photocatalytic activity of ZnO is affected by the fast recombination of the photogenerated charge carriers which reduces the efficiency of the photocatalytic processes. In order to overcome this problem, simultaneous doping with two kinds of atoms [15,16] or coupling ZnO with other semiconductors of suitable electronic properties [17–47] have been found to be a viable strategy to increase the charge separation of the photogenerated electron/hole pairs. For this reason, many coupled semiconductor systems have been proposed as photocatalysts such as ZnO–TiO_2 [17–19], ZnO–CdS [20,21], ZnO–AgBr [22], ZnO–Ag_2S [23]. In particular, ZnO–SnO_2 coupled oxides [24–47] have been largely studied to ameliorate the photocatalytic activity of ZnO. The performance of each system depends essentially on the position of the conduction and valence bands of the two semiconductors which directly influences the separation and the recombination of the photogenerated e^-/h^+ pairs [48].

Tennakone and Bandara were the first to investigate ZnO–SnO_2 composites as potential photocatalysts for the sensitized degradation of dyes [24,25]. Their catalytic activity was superior to that

* Corresponding author. Tel.: +39 91 238 63729; fax: +39 702 5020.
E-mail addresses: hamrouni-28@hotmail.fr (A. Hamrouni), agatino.dipaola@unipa.it (A. Di Paola).

http://dx.doi.org/10.1016/j.molcata.2014.03.018
1381-1169/

of individual ZnO or SnO_2 and was attributed to the wider charge separation ability of the composite system. Other researchers [24–30,34,42] related the enhanced photocatalytic properties of the ZnO–SnO_2 systems to the vectorial transfer of electrons and holes between ZnO and SnO_2 but only recently this hypothesis has been confirmed by determination of the band alignment of the ZnO–SnO_2 heterostructure by X-ray photoelectron spectroscopy [45].

Coupled ZnO/SnO_2 photocatalysts have been obtained by a variety of different processes. The most common method was the heterogeneous co-precipitation from aqueous solutions of $ZnSO_4$ and $SnCl_4$ using NaOH [26–28] or NH_3•H_2O [29,47]. Nanosized ZnO/SnO_2 samples were synthesized by homogeneous co-precipitation using ethyl acetate as precipitating agent [31] or by fractional homogeneous co-precipitation using urea as the latent precipitant under boiling reflux conditions [43]. Yang et al. [41] prepared ZnO/SnO_2 composites via cetyltrimethylammonium bromide assisted co-precipitation starting from $Zn(NO_3)_2$ and $SnCl_4$ solutions. Recently, a novel method employed the high-gravity reactive precipitation using a rotating packed bed [44].

Other methods for preparing ZnO–SnO_2 photocatalysts included the hydrothermal method using an aqueous solution containing ZnO rods, $SnCl_4$ and NaOH [32] or a mechanochemical processing of anhydrous chloride precursors with Na_2CO_3 [30]. Uddin et al. [45] prepared nanoporous ZnO–SnO_2 photocatalysts by a two step procedure involving the homogeneous precipitation of SnO_2 particles combined with a hydrothermal treatment and the reaction of the as-prepared SnO_2 particles with zinc acetate. Network structured ZnO/SnO_2 samples were synthesized by a two-step solvothermal method [35].

Only few works have concerned the employment of the sol–gel method to obtain ZnO/SnO_2 composites [36–40]. In particular, Zhenya et al. [36] used $Zn(CH_3COO)_2{\cdot}2H_2O$, oxalic acid and $SnCl_2{\cdot}2H_2O$ as raw materials and the samples were treated under high pressure at 6 GPa. One-dimensional ZnO–SnO_2 nanofibers were synthesized by combination of sol–gel process and electrospinning technique [37]. Prevalently, the sol–gel dip coating technique was used to prepare ZnO/SnO_2 thin films using zinc acetate and $SnCl_4$ dissolved in CH_3OH [39] or $CH_3COCH_2COCH_3$ and $CH_3OC_2H_4OH$ [41]. Recently, Torres Martínez et al. [40] studied the antibacterial performance of thin films prepared from mixtures of $Zn(CH_3COO)_2{\cdot}2H_2O$, and $SnCl_2{\cdot}2H_2O$ dissolved in ethylene glycol and ethanol solutions, respectively.

In a previous study Hamrouni et al. [47] demonstrated that ZnO–SnO_2 nanocomposites, prepared with the co-precipitation method, were more efficient than the corresponding pure oxides. The aim of this study was to further improve the photocatalytic activity of the ZnO–SnO_2 coupled catalysts. ZnO–SnO_2 powders were prepared by a novel facile sol–gel synthesis route. The samples were tested for the photodegradation of 4-nitrophenol (4-NP) under UV-light irradiation in solid-liquid phase. 4-NP was chosen as a probe molecule for the photocatalytic runs because substituted phenols are ubiquitous contaminants in water streams [49]. The influence of the calcination temperature and the ZnO/SnO_2 molar ratio was investigated. A morphological and photoelectrochemical investigation was carried out in order to establish a correlation between ZnO–SnO_2 heterojunction effect and enhanced photocatalytic activity. For the first time, the proposed charge transfer mechanism between ZnO and SnO_2 was based on the experimental determination of the position of the conduction and valence bands of the two semiconductors by means of photovoltage measurements carried out in slurry systems. These data, strictly related to the real reaction conditions, are more reliable than those obtained with other methods reported in literature [39,50].

2. Experimental

2.1. Synthesis

Zinc acetate dihydrate (Sigma–Aldrich) and tin chloride pentahydrate (Sigma–Aldrich) were used as starting materials. Methanol (Sigma–Aldrich) and 28% ammonium hydroxide solution (Fluka) were used as solvent and additive, respectively. All the chemical products were used as received without any further purification. The synthesis of the ZnO–SnO_2 mixed photocatalysts started by slowly adding a 0.1 M methanol solution of $Zn(CH_3COO)_2{\cdot}2H_2O$, previously prepared at 70 °C under vigorous stirring, to a 0.1 M methanol solution of $SnCl_4{\cdot}5H_2O$ prepared in the same conditions. Tipically, 8.12 g of $Zn(CH_3COO)_2{\cdot}2H_2O$ were dissolved in 370 ml of methanol and the amount of $SnCl_4{\cdot}5H_2O$ solution was opportunely determined in order to obtain powders with molar ratio ZnO/SnO_2 equal to 1/0.02, 1/0.05, 1/0.25 labeled as $ZnSn_{0.02}$, $ZnSn_{0.05}$ and $ZnSn_{0.25}$, respectively. The obtained solutions were continuously stirred for 2 h, keeping the temperature at 70 °C. Then, the NH_4OH solution was added dropwise until pH reached the value of 8. The solutions became gels which were dried for 20 h at 110 °C to produce xerogels. Finally, the photocatalysts were obtained by calcining the xerogels for 2 h at different temperatures (500, 600 and 700 °C). The pure oxides were synthesized in the same way by using only the corresponding precursors.

2.2. Characterization

X-ray diffraction patterns of the powders were recorded at room temperature by an Ital Structures APD 2000 powder diffractometer using the Cu K_α radiation and a 2θ scan rate of 2°/min. The mean grain size of the photocatalysts was estimated using the Debye–Scherrer equation:

$$D = \frac{0.9\lambda}{\beta \cos\theta} \quad (1)$$

where D is the mean grain size (nm), λ is the wavelength of the X-ray radiation (0.154 nm), β is the corrected full width at half maximum height and θ is the diffraction angle. The specific surface area (SSA) of the samples was determined with a Micrometrics Flow Sorb 2300 instrument by using the single-point BET method. UV–vis diffuse reflectance spectra (DRS) of the samples were recorded by using a Shimadzu UV-2401PC spectrophotometer. $BaSO_4$ was used as a reference and the spectra were recorded in the range 200–800 nm.

The morphology of the catalyst was examined using a Philips XL30 ESEM scanning electron microscope (SEM), operating at 30 kV on specimens upon which a thin layer of gold was deposited. Transmission electron microscopy (TEM) measurements were obtained using a JEM-2100 (JEOL, Japan) operating at 200 kV accelerating voltage, equipped with an energy dispersive X-ray spectrometer (EDS, Oxford, UK) suitable for element identification. The powders were dispersed in isopropanol and a small drop was deposited on a 200 mesh carbon-coated copper grid, which was introduced into the TEM chamber analysis after complete solvent evaporation.

X-ray photoelectron spectroscopy (XPS) analyses were performed with a VG Microtech ESCA 3000 Multilab equipped with a dual Mg/Al anode. The spectra were excited by the non-monochromatised Al Ka source (1486.6 eV) run at 14 kV and 15 mA.

2.3. Photovoltage and photoluminescence measurements

Photovoltage measurements were performed in a Pyrex reactor with a total volume of 150 mL. 100 mg of photocatalyst were added to 100 mL of a 0.1 M $NaNO_3$ solution. A platinum electrode was used as working electrode and the reference was an Ag/AgCl

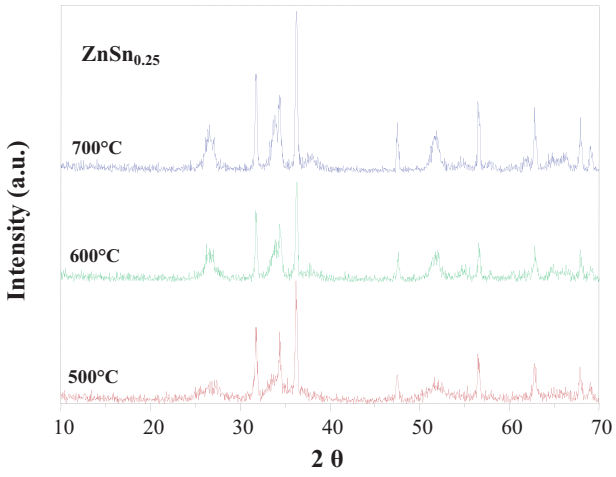

Fig. 1. XRD patterns of $ZnSn_{0.25}$ calcined for 2 h at different temperatures.

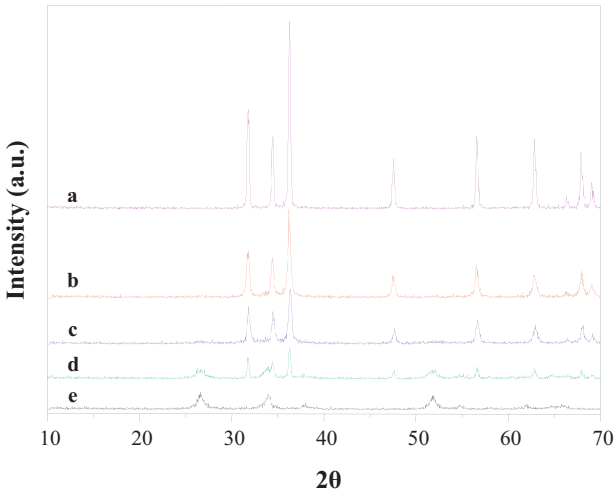

Fig. 2. XRD patterns of (a) pure ZnO, (b) $ZnSn_{0.02}$, (c) $ZnSn_{0.05}$, (d) $ZnSn_{0.25}$ and (e) pure SnO_2, calcined at 600 °C for 2 h.

electrode. After degassing for 30 min with N_2, 20 mg of methyl viologen (1,1′-dimethyl-4,4′-bipyridinium dichloride) were added to the suspension. Then, the mixture was once more degassed for 30 min. The pH was adjusted using HNO_3 and NaOH solutions. During the experiments, the suspension was irradiated by two UV lamps (Philips HPK 125 W). The values of pH and potential (V) were measured using a pH meter Thermo Orion 720A and a multimeter Metex 3800, respectively.

Photoluminescence spectra were recorded at room temperature with a Jobin Yvon Spex Fluoromax II spectrofluorimeter equipped with a Hamamatsu R3896 photomultiplier.

2.4. Photocatalytic experiments

A cylindrical Pyrex batch photoreactor containing 0.15 L of the 4-NP solution (20 mg/L) was used to carry out the photodegradation experiments. For each photocatalytic run, the amount of photocatalyst was chosen in order to ensure that almost all the photons emitted by the lamp were absorbed from the suspension. A 125 W medium pressure Hg lamp (Helios Italquartz, Italy) with a maximum emission at about 365 nm was axially positioned within the photoreactor. The photon flux emitted by the lamp was $\Phi_i = 14\ mW\ cm^{-2}$. The temperature of the solution was controlled by circulation of water through a Pyrex thimble surrounding the lamp. A magnetic stirrer was used to guarantee the homogeneity of the reacting mixture. Before the light was turned on, the suspension was kept in the dark for 2 h to reach the adsorption–desorption equilibrium. Samples were taken at different time intervals to evaluate the progress of the degradation of 4-NP. Each sample was filtered by a 0.2 μm filter and the residual 4-NP concentration was measured by the UV–vis spectrophotometer. Total organic carbon (TOC) analyses were performed using a Shimadzu 5000A TOC analyser; each sample was analyzed three times and the average values were reported.

3. Results

3.1. Structural and morphological characterization

Preliminary tests were carried out to find the calcination temperature that ensured the best compromise between crystallinity and surface area of the catalysts. Fig. 1 shows X-ray diffraction patterns of the $ZnSn_{0.25}$ sample calcined at 500, 600 and 700 °C. The peaks were found to be relative to ZnO with hexagonal wurtzite structure (JCPDS card number: 36-1451) and SnO_2 with tetragonal structure (JCPDS card number: 41-1445) and no other phases were detected. ZnO was well crystallized already at 600 °C whereas SnO_2 was almost amorphous at 600 °C and its crystallinity increased with the calcination temperature. The average grain sizes of the various samples were determined by using the diffraction peaks (1 0 1) for ZnO and (1 1 0) for SnO_2. As shown in Table 1, the main grain sizes of ZnO and SnO_2 increased with the calcination temperature and, correspondingly, the specific surface area of $ZnSn_{0.25}$ decreased.

Fig. 2 shows the diffractograms of pure ZnO, pure SnO_2 and various ZnO–SnO_2 samples calcined at 600 °C. The crystallinity degree of ZnO decreased with increasing the amount of SnO_2 in agreement with previous results obtained for coupled ZnO/SnO_2 photocatalysts prepared by co-precipitation [26,27,44]. The peaks related to SnO_2 were detected in $ZnSn_{0.25}$ but were very small for $ZnSn_{0.05}$ and not appreciable for $ZnSn_{0.02}$. This can be due both to the small amount of SnO_2 present which remained below the detection limit of the instrument and/or to the very low crystallinity of SnO_2 which appeared almost amorphous after calcination at 600 °C. It is worth noting that all the samples obtained were more pure and crystalline than those synthesized by the co-precipitation method [47].

Mixing two different oxides generally limits the growth of both. As shown in Table 1, at the same calcination temperature the mean sizes of ZnO and SnO_2 were larger in the single oxides than in the mixed ZnO–SnO_2 samples. The addition of SnO_2 caused a reduction of the main crystallite size of ZnO. This finding is consistent with literature results reporting that the inhibition of the growth of ZnO increased with increasing the SnO_2 content [26,27,47]. The specific surfaces areas of the mixed samples were higher than that of ZnO, lower than that of SnO_2 and increased with the Sn content (see Table 1).

SEM observations revealed that all the samples consisted of aggregates of particles whose average sizes appeared quite close to those calculated from the XRD patterns. As shown in Fig. 3a, the particles of pure ZnO had a hexagonal shape whereas the particles of SnO_2 (Fig. 3b) showed a sphere-like morphology. The micrographs of the mixed ZnO–SnO_2 samples revealed the presence of both morphologies. Fig. 3c and d show the representative SEM images of $ZnS_{0.05}$ and $ZnS_{0.25}$, respectively. The small crystallites of the different phases were interwoven with each other forming tightly bound nanoclusters.

The surface structure of the mixed ZnO–SnO_2 samples was investigated by XPS. The survey spectrum revealed the presence of O, Sn and Zn. Fig. 4 shows the high resolution spectra of the Zn and Sn species, respectively. The peak centered at 1021.6 eV (Fig. 4a) was attributed to Zn $2p_{3/2}$ of Zn(II) [51]. The peaks located at 487.1

Table 1
Physical characteristics of pure ZnO, pure SnO_2 and ZnO–SnO_2 nanocomposites.

	ZnO (600 °C/2 h)	SnO_2 (600 °C/2 h)	$ZnSn_{0.02}$ (600 °C/2 h)	$ZnSn_{0.05}$ (600 °C/2 h)	$ZnSn_{0.25}$ (500 °C/2 h)	$ZnSn_{0.25}$ (600 °C/2 h)	$ZnSn_{0.25}$ (700 °C/2 h)
Mean size of ZnO (nm)	34.8	–	26.1	17.5	13.5	15.0	29.0
Mean size of SnO_2 (nm)	–	10.2	–	–	6.8	7.5	34.0
SSA (m^2/g)	4.2	26.9	10.0	22.4	24.4	22.8	19.8
Band gap (eV)	3.20	3.55	3.15	3.10	3.19	3.18	3.19

and 495.5 eV (Fig. 4b) were assigned to Sn $3d_{5/2}$ and Sn $3d_{3/2}$ of Sn(IV) [52]. These results confirmed that the oxidation states of Zn and Sn were +2 and +4, respectively, in agreement with the XRD results.

Fig. 5 shows the results of TEM observations of the $ZnSn_{0.05}$ sample. Energy dispersive spectroscopy (EDS) analysis confirmed that the sample consisted of Zn, Sn and O (copper came from the grid of the sample holder) which is consistent with the XRD and XPS results (Fig. 5a). According to the TEM image of Fig. 5b, the sample was composed of nanoparticles with sizes in the range of about 30–80 nm and each nanoparticle was attached to several other nanoparticles. The high-resolution image of Fig. 5c evidenced the presence of intergrown lattices of ZnO and SnO_2.

3.2. DRS spectroscopy

Fig. 6A shows the UV–vis absorption spectra of the various samples calcined at 600 °C. ZnO presented the highest absorbance values in the UV region whilst SnO_2 revealed a low intensity absorbance due probably to its poor crystallinity. The absorbance of the mixed samples progressively decreased with increasing the content of SnO_2.

The band gap values (E_g) of the photocatalysts were estimated by extrapolation of the linear part of the plots of $(\alpha h\nu)^2$ vs the energy of the exciting light (see Fig. 6B) assuming that all the samples were direct crystalline semiconductors [53]. As shown in Table 1, the E_g values of ZnO and SnO_2 were 3.20 and 3.55 eV, respectively. The band gap values of the samples containing ZnO and SnO_2 ranged between 3.10 and 3.19 eV and were lower than those of both pure oxides independently on the Zn/Sn molar ratio investigated. In any case the band gap energy was very close to that of bare ZnO being the amount of SnO_2 relatively low.

The influence of the temperature on the band gap energy was negligible being the values obtained for the sample $ZnSn_{0.25}$ at 500, 600 and 700 °C almost the same.

3.3. Photovoltage and photoluminescence measurements

The values of the flat-band potentials of the ZnO and SnO_2 samples were determined by the slurry method proposed by Roy et al. [54], measuring the variation of the photovoltage with the pH of suspensions of the powders in the presence of an electron acceptor. Fig. 7 shows the photovoltage vs pH curves obtained by irradiation of ZnO and SnO_2 suspensions in the presence of methyl viologen dichloride. It was not possible to adjust the pH below 5 (to measure the photovoltage for pH lower than 5) because ZnO dissolves under these conditions.

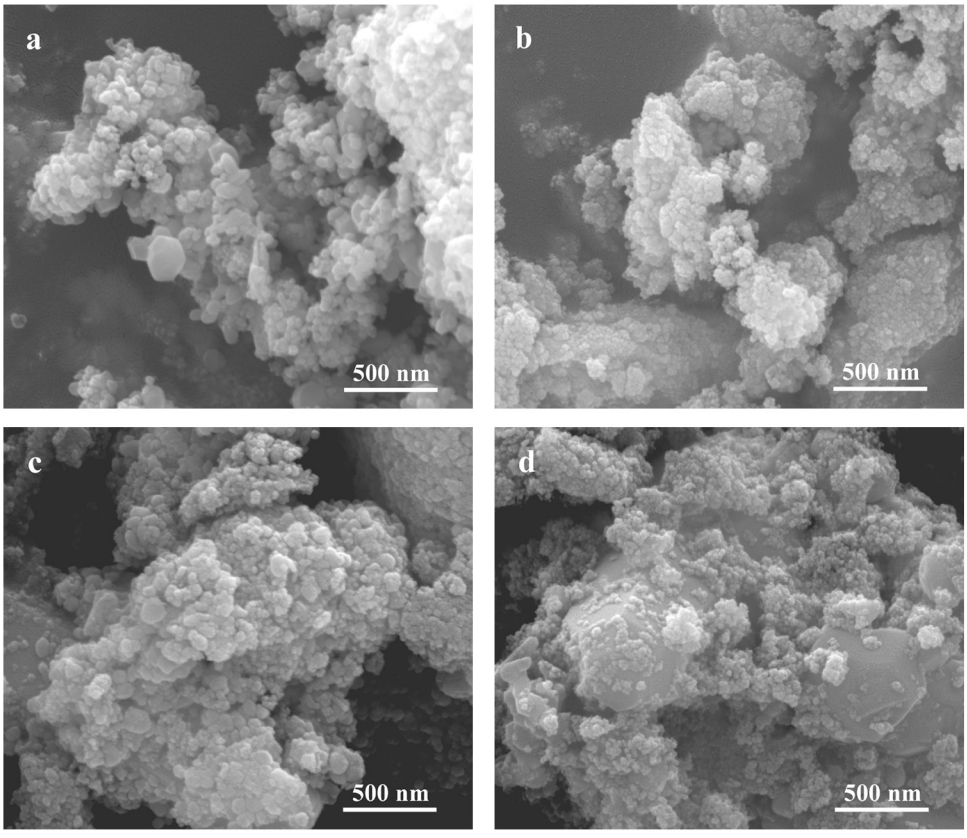

Fig. 3. SEM micrographs of (a) ZnO, (b) SnO_2, (c) $ZnSn_{0.05}$, (d) $ZnSn_{0.25}$ calcined at 600 °C for 2 h.

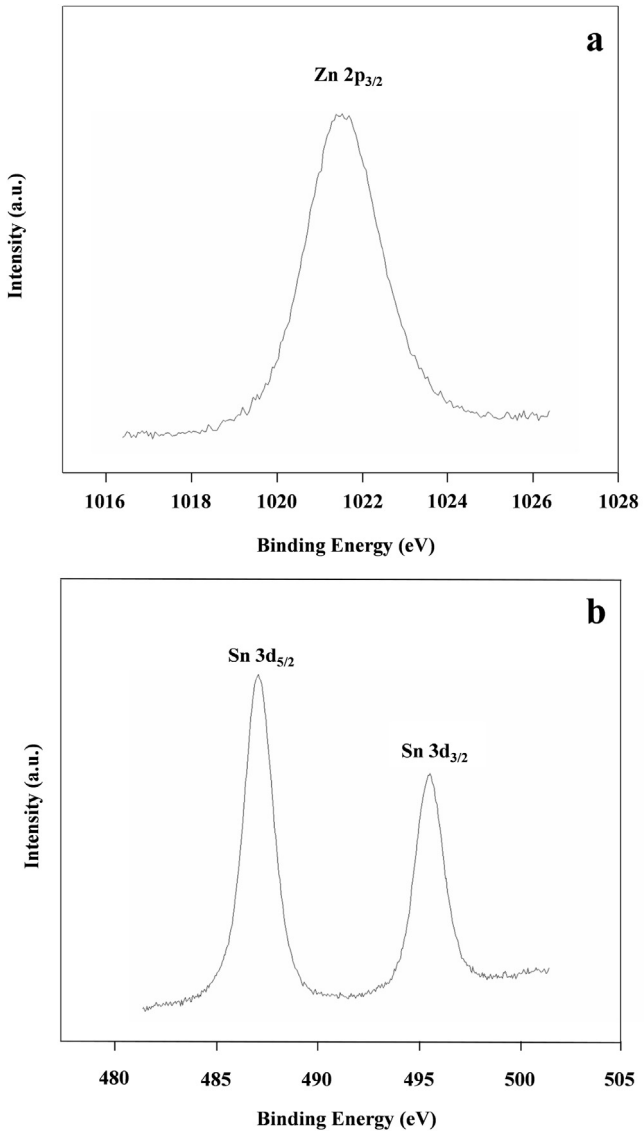

Fig. 4. XPS spectra of the $ZnSn_{0.25}$ sample: (a) Zn 2p region; (b) Sn 3d region.

The pH value of the inflection point (pH_0) of the obtained sigmoidal titration curves allows to calculate the flat band potential at pH 7 by the equation:

$$E_{FB}(pH = 7) = E^0_{MV^{2+}/MV^{+\bullet}} + 0.059(pH_0 - 7) \quad (2)$$

where $E^0_{MV^{2+}/MV^{+\bullet}}$ is the standard potential of the redox couple $MV^{2+}/MV^{+\bullet}$ equal to −0.445 V vs (NHE) [55]. The values obtained were −0.36 and −0.11 V for ZnO and SnO_2, respectively. These values are in good accordance with the flat band potentials of −0.48 V for ZnO and −0.21 V for SnO_2, reported by Butler et al. [50].

Fig. 8 shows the photoluminescence (PL) spectra of bare ZnO and $ZnSn_{0.05}$. The PL spectrum of ZnO was characterized by a narrow ultraviolet peak at 380 nm. Coupling SnO_2 with ZnO led to a decrease of PL intensity. Similar results were obtained by Asokan et al. [56] who synthesized nanocomposite ZnO–SnO_2 nanofibers by an electrospinning method.

Photoluminescence originates from the radiative recombination of photogenerated electron–hole pairs [57]. The different position of the respective conduction bands of ZnO and SnO_2 allows the photogenerated electrons migrate from the conduction band of ZnO

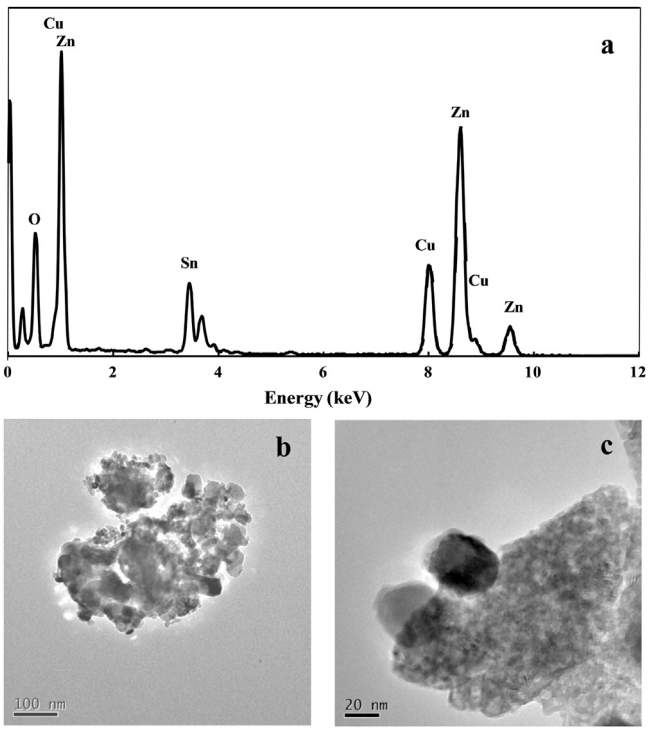

Fig. 5. (a) EDS spectrum and (b, c) TEM images of $ZnSn_{0.05}$.

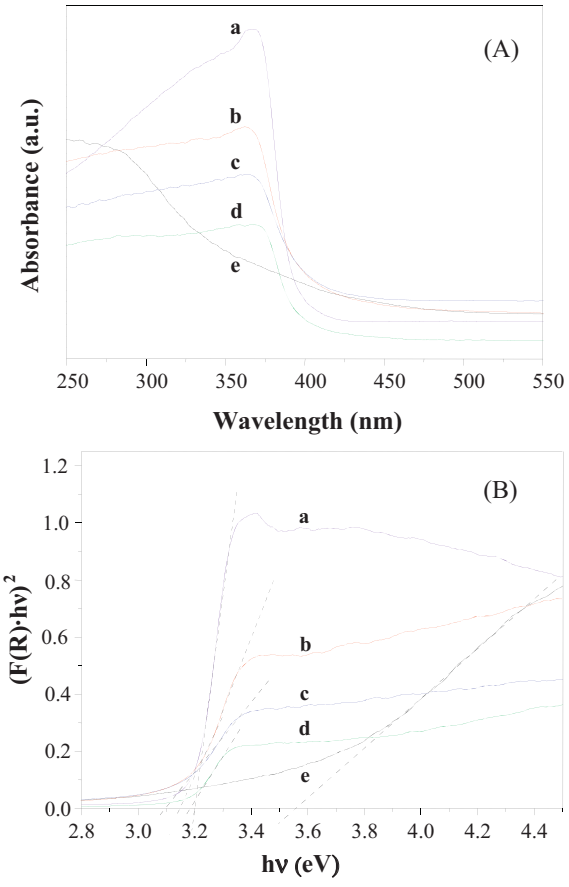

Fig. 6. UV–vis absorption spectra (A) and plots of $(F(R)\,h\nu)^2$ vs $h\nu$ (B) of: (a) pure ZnO, (b) $ZnSn_{0.02}$, (c) $ZnSn_{0.05}$, (d) $ZnSn_{0.25}$ and (e) pure SnO_2.

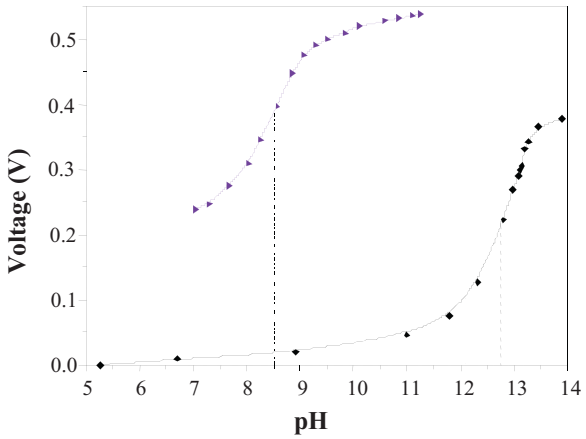

Fig. 7. Effect of pH on the photovoltage developed by irradiation of (►) pure ZnO, and (♦) pure SnO_2 calcined at 600 °C for 2 h.

to that of SnO_2, reducing the recombination of the photoinduced electrons on the ZnO surface and weakening the PL signal.

3.4. Photocatalytic activity

The photocatalytic activity of the powders was investigated by following the degradation of 4-NP under UV light. Fig. 9 shows the kinetics of photodegradation of 4-NP in the presence of the various samples calcined at 600 °C for 2 h. The reaction rate constant, *k*, was calculated from the initial slope of the concentration vs time profiles. The *k* values are reported in Table 2.

The photocatalytic activity of SnO_2 was very low compared to that of ZnO but all the ZnO–SnO_2 samples were more active than the two pure oxides showing that the contemporaneous presence of two phases resulted in a synergistic effect. In particular, $ZnSn_{0.05}$ revealed the highest photocatalytic efficiency.

Fig. 10 shows the effect of the calcination temperature on the photocatalytic activity of the $ZnSn_{0.25}$ sample. The best efficiency was obtained when the sample was calcined at 600 °C whereas the powders calcined at 500 and 700 °C were less active. This result is mainly due to two opposite effects: growth of the size of the particles leading to a low surface area and increase of the cristallinity with the temperature. The sample calcined at 500 °C has the highest SSA (24.4 m^2/g) but it is the least crystalline. Instead, the sample calcined at 700 °C is the most crystalline but it has the lowest specific surface area (19.8 m^2/g).

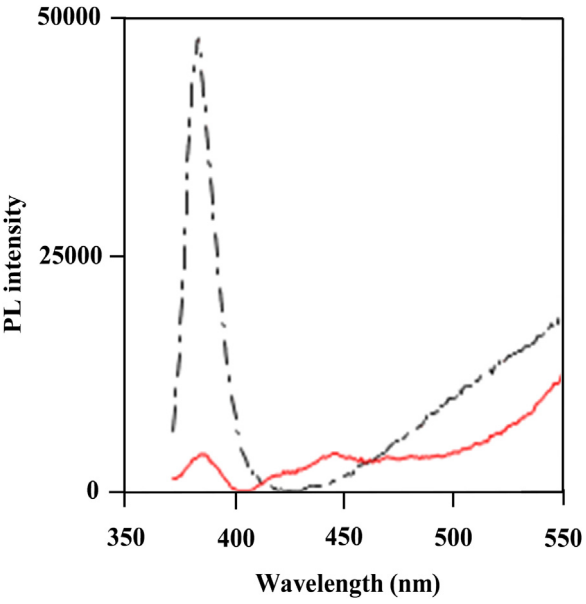

Fig. 8. Photoluminescence spectra of pure ZnO (dash-dotted line) and $ZnSn_{0.05}$ (solid line).

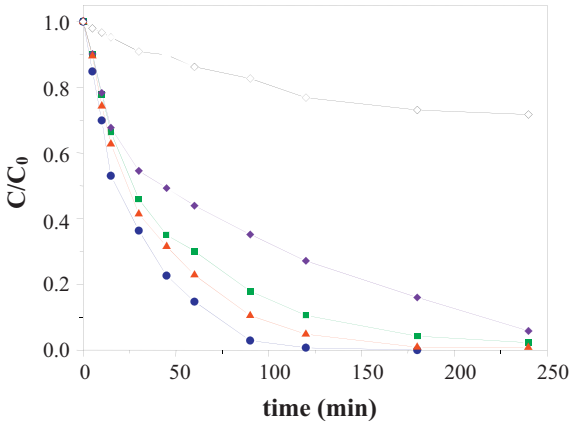

Fig. 9. Degradation kinetics of 4-NP over: (◊) SnO_2, (♦) ZnO, (▲) $ZnSn_{0.02}$, (●) $ZnSn_{0.05}$ and (■) $ZnSn_{0.25}$ calcined at 600 °C for 2 h.

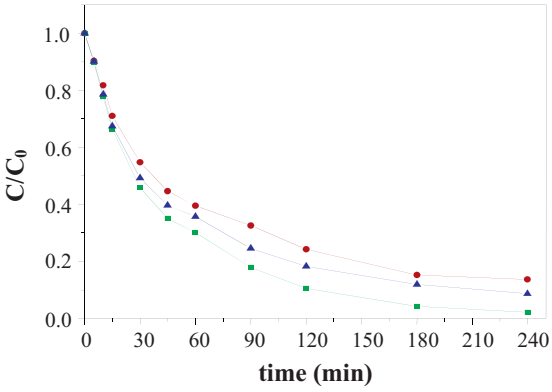

Fig. 10. Degradation kinetics of 4-NP over $ZnSn_{0.25}$ calcined for 2 h at: (●) 500, (■) 600 and (▲) 700 °C.

Fig. 11 shows the total organic carbon elimination kinetics in the presence of $ZnSn_{0.05}$. It is worth noting that about 40% of TOC remained when 4-NP totally disappeared. After 240 min, more than 20% of organic carbon was still present in the system due to the formation of long-lived by-products [58,59]. Anyway, the complete mineralization of the substrate was reached after a longer time.

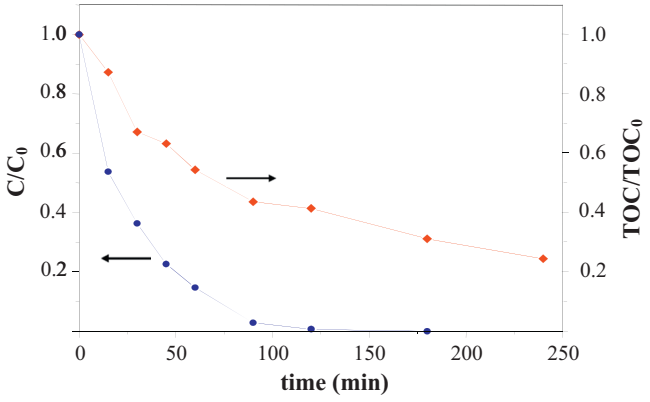

Fig. 11. Degradation (●) and total organic elimination (♦) kinetics of 4-NP over $ZnSn_{0.05}$ calcined for 2 h at 600 °C.

Table 2
Photodegradation rate constants of 4-NP on pure ZnO, pure SnO_2 and ZnO–SnO_2 photocatalysts.

	ZnO (600 °C/2 h)	SnO_2 (600 °C/2 h)	$ZnSn_{0.02}$ (600 °C/2 h)	$ZnSn_{0.05}$ (600 °C/2 h)	$ZnSn_{0.25}$ (500 °C/2 h)	$ZnSn_{0.25}$ (600 °C/2 h)	$ZnSn_{0.25}$ (700 °C/2 h)
$k \times 10^3$ (min^{-1})	25.2	3.3	30.2	40.0	22.0	26.4	25.2

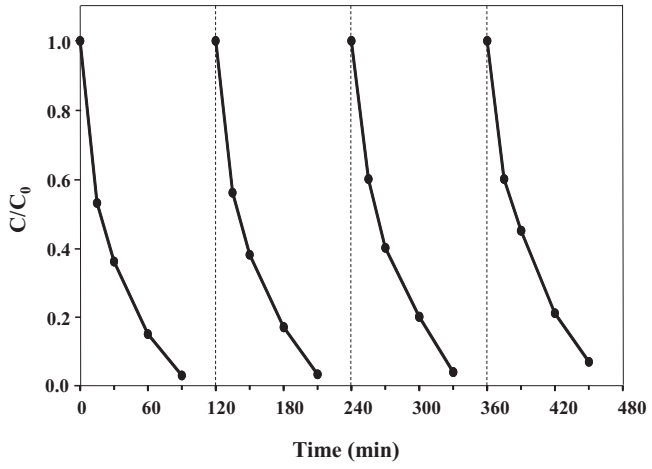

Fig. 12. Reusability tests of $ZnSn_{0.05}$.

Fig. 12 shows the results obtained after reuse of $ZnSn_{0.05}$. After each photocatalytic run, the powder was recuperated, washed with distilled water and a fresh solution of 4-NP was added. Although the degradation efficiency slightly decreased after each run, the ZnO–SnO_2 catalyst remained effective and reusable under UV light irradiation.

Fig. 13 shows a comparison between the kinetics of degradation of 4-NP in the presence of $ZnS_{0.05}$ samples synthesized by two different methods. The ZnO–SnO_2 photocatalyst prepared by the sol–gel method revealed a photocatalytic activity higher than that of the sample prepared by the conventional co-precipitation method [47].

4. Discussion

The high photocatalytic activity of the ZnO–SnO_2 nanocomposites with respect to the pure oxides can be explained by the contemporaneous presence of two semiconductors possessing different energy levels for their corresponding conduction and valence bands. Depending on the potentials of the photogenerated holes and electrons, it is possible a vectorial transfer of charge carriers from a semiconductor to another, leading to more efficient electron–hole separation and higher photocatalytic activity [48].

Both ZnO and SnO_2 are n-type semiconductors so that, assuming that the difference between flat band potential and conduction band edge is negligible, it is possible to locate the valence band edge of ZnO and SnO_2 by adding the band gap energy to the flat-band potential value. The results have shown that the valence band of ZnO (E_{VB} = 2.84 eV) is lower than that of SnO_2 (E_{VB} = 3.44 eV). Similarly, the conduction band of ZnO (E_{CB} = −0.36 eV) is lower than that of SnO_2 (E_{CB} = −0.11 eV). Fig. 14 shows a schematic diagram of the energy band structures of ZnO and SnO_2 at pH = 7. Although these data may not be the exact absolute values of the conduction and valence band potentials of ZnO and SnO_2, they should offer a correct estimation of the relative band edge positions of the two semiconductors.

When the ZnO–SnO_2 nanocomposites are irradiated by UV light, electrons can transfer from the more cathodic conduction band of ZnO to the more anodic conduction band of SnO_2. Analogously, holes transfer can occur from the valence band of SnO_2 to the valence band of ZnO. The efficient charge separation can increase the lifetime of the charge carriers and enhance the efficiency of the interfacial charge transfer to adsorbed substrates. The inhibition of the electron–hole recombination is confirmed by the PL spectra of the mixed ZnO–SnO_2 samples that revealed a weakening of the PL intensity with respect to that of pure ZnO. A mechanistic scheme of the charge separation in the ZnO–SnO_2 system is shown in Fig. 14.

The enhanced photoactivity of the ZnO–SnO_2 nanocomposites is so attributable to the formation of local heterojunctions between

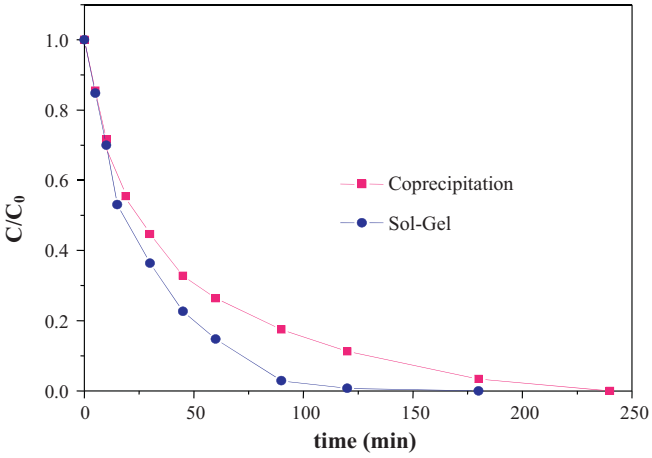

Fig. 13. Degradation kinetics of 4-NP over $ZnSn_{0.05}$ samples calcined for 2 h at 600 °C, synthesized by different methods.

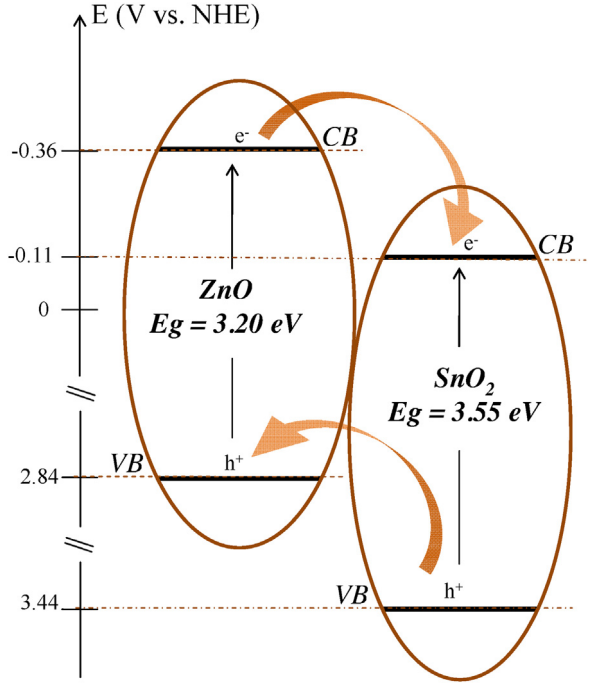

Fig. 14. Schematic diagram representing the charge-transfer processes between coupled ZnO–SnO_2 particles.

ZnO and SnO_2 particles which facilitate the separation of the photogenerated e^-/h^+ pairs. The photocatalytic efficiency is related to the number of different particles attached to each other that depends on the ZnO/SnO_2 molar ratio. As shown by the XRD and TEM results, the SnO_2 particles present in the $ZnSn_{0.02}$ and $ZnSn_{0.05}$ samples are probably very small and finely dispersed on the surface of the ZnO particles so that a large number of heterojunctions may exist: this justifies the enhanced photoactivity of the coupled ZnO–SnO_2 samples with respect to pure ZnO. With increasing the content of SnO_2 the photoactivity decreases due to the presence of large crystals of SnO_2 that reduces the number of heterojunctions and/or to the increase of free SnO_2 particles that have poor photocatalytic activity. Therefore, there is an optimum SnO_2 content that leads to a maximum photocatalytic efficiency.

A comparison of the data reported in Tables 1 and 2 shows that there is a correspondence between the E_g values of the ZnO–SnO_2 nanocomposites and the photocatalytic results. In particular, the photodegradation rate constants of 4-NP increased with decreasing the band gap values of the mixed samples. In agreement con previous results obtained with various coupled semiconductors [40,60–63], $ZnSn_{0.05}$, which presented the lowest band gap value, was the most active sample.

The experimental results have shown that the coupled ZnO–SnO_2 samples synthesized with the sol–gel method were more crystalline and with a mean particle size smaller than that of the samples obtained by co-precipitation at the same calcination temperature [47]. Besides, the particles synthesized with the sol–gel method revealed a sphere-like morphology whereas the co-precipitated particles had a plate-like form [47]. The highest photocatalytic activity of the sol–gel prepared samples can be so ascribed not only to the enhanced cristallinity but also to the smaller size and the more regular form of the single particles that allow the formation of a larger amount of heterojunctions. A similar effect of the differences of particle size was reported by Zhang et al. [29] who compared the photoefficiency of coupled ZnO–SnO_2 samples prepared by co-precipitation using $NH_3 \cdot H_2O$ as the precipitant with samples obtained using NaOH.

5. Conclusion

ZnO–SnO_2 nanocomposite photocatalysts have been synthesized with a facile sol–gel route. The photoefficiency of the ZnO–SnO_2 samples was superior to that of pure ZnO or SnO_2. The photocatalytic activity was found to be dependent on the calcination temperature and on the ZnO/SnO_2 molar ratio. $ZnSn_{0.05}$ revealed the highest efficiency for the degradation of 4-NP. The enhanced photoactivity was attributed to the charge separation of the photoproduced electron/hole pairs arising from the coupling of ZnO with SnO_2. The small size of the particles and the intimate contact with each other are crucial factors to increase the efficiency of the samples.

Acknowledgements

This work was financially supported by MIUR (Rome). The authors thank Dr. Anna Maria Venezia of ISMN-CNR (Palermo) and Dr. Rossano Amadelli of ISOF-CNR (Ferrara) for the XPS and PL measurements, respectively. HR-TEM experimental data were provided by Centro Grandi Apparecchiature – UniNetLab – Università di Palermo funded by P.O.R. Sicilia 2000–2006, Misura 3.15 Quota Regionale. The authors thank the minister of Higher Education and Scientific Research, Tunisia, for the fellowship awarded to A. Hamrouni.

References

[1] A. Fujishima, K. Honda, Nature 238 (1972) 37–38.
[2] J.M. Hermann, J. Photochem. Photobiol. A: Chem. 216 (2010) 85–93.
[3] A. Houas, H. Lachheb, M. Ksibi, E. Elaloui, C. Guillard, J.M. Herrmann, Appl. Catal. B: Environ. 31 (2001) 145–157.
[4] K. Nakata, A. Fujishima, J. Photochem. Photobiol. C: Rev. 13 (2012) 169–189.
[5] A. Di Paola, E. Garcia-López, G. Marcì, L. Palmisano, J. Hazard. Mater. 211 (2012) 3–29.
[6] S.J. Pearton, D.P. Norton, K. Ip, Y.W. Heo, T. Steiner, Prog. Mater. Sci. 50 (2005) 293–340.
[7] M. Miyauchi, A. Nakajima, T. Watanabe, K. Hashimoto, Chem. Mater. 14 (2002) 2812–2816.
[8] E. Yassitepe, H.C. Yatmaz, C. Öztürk, K. Öztürk, C. Duran, J. Photochem. Photobiol. A: Chem. 198 (2008) 1–6.
[9] N. Daneshvar, D. Salari, A.R. Khataee, J. Photochem. Photobiol. A: Chem. 162 (2004) 317–322.
[10] G. Colón, M.C. Hidalgo, J.A. Navío, E. Pulido Melián, O. González Díaz, J.M. Doña Rodríguez, Appl. Catal. B. Environ. 83 (2008) 30–38.
[11] S. Sakthivel, B. Neppolian, M.V. Shankar, B. Arabindoo, M. Palanichamy, V. Murugesan, Sol. Energy Mater. Sol. Cells 77 (2003) 65–82.
[12] B. Krishnakumar, M. Swaminathan, Indian J. Chem. 49 (2010) 1035–1040.
[13] B. Krishnakumar, K. Selvam, R. Velmurugan, M. Swaminathan, Desal. Water Treat. 24 (2010) 132–139.
[14] B. Krishnakumar, M. Swaminathan, Spectrochim. Acta A 81 (2011) 739–744.
[15] B. Subash, B. Krishnakumar, R. Velmurugan, M. Swaminathan, M. Shanthi, Catal. Sci. Technol. 2 (2012) 2319–2326.
[16] B. Subash, B. Krishnakumar, M. Swaminathan, M. Shanthi, Langmuir 29 (2013) 939–949.
[17] G. Marcì, V. Augugliaro, M.J. López-Munõz, C. Martín, L. Palmisano, V. Rives, M. Schiavello, R.J.D. Tilley, A.M. Venezia, J. Phys. Chem. B 105 (2001) 1033–1040.
[18] G. Marcì, V. Augugliaro, M.J. López-Munõz, C. Martín, L. Palmisano, V. Rives, M. Schiavello, R.J.D. Tilley, A.M. Venezia, J. Phys. Chem. B 105 (2001) 1026–1032.
[19] C. Shifu, Z. Wei, L. Wei, Z. Sujuan, Appl. Surf. Sci. 255 (2008) 2478–2484.
[20] S. Sakthivel, S.U. Geissen, D.W. Bahnemann, V. Murugesan, A. Vogelpohl, J. Photochem. Photobiol. A: Chem. 148 (2002) 283–293.
[21] J. Nayak, S.N. Sahu, J. Kasuya, S. Nozaki, Appl. Surf. Sci. 254 (2008) 7215–7218.
[22] B. Krishnakumar, B. Subash, M. Swaminathan, Sep. Purif. Technol. 85 (2012) 35–44.
[23] B. Subash, B. Krishnakumar, V. Pandiyan, M. Swaminathan, M. Shanthi, Sep. Purif. Technol. 96 (2012) 204–213.
[24] K. Tennakone, J. Bandara, Appl. Catal. A: Gen. 208 (2001) 335–341.
[25] J. Bandara, K. Tennakone, P.P.B. Jayatilaka, Chemosphere 49 (2002) 439–445.
[26] C. Wang, J. Zhao, X. Wang, B. Mai, G. Sheng, P. Peng, J. Fu, Appl. Catal. B: Environ. 39 (2002) 269–279.
[27] C. Wang, X. Wang, B. Xu, J. Zhao, B. Mai, P. Peng, G. Sheng, J. Fu, J. Photochem. Photobiol. A: Chem. 168 (2004) 47–52.
[28] T. An, M. Zhang, X.M. Wang, G.Y. Sheng, J.M. Fu, J. Chem. Technol. Biotechnol. 80 (2005) 251–258.
[29] M. Zhang, T. An, X. Hu, C. Wang, G. Sheng, J. Fu, Appl. Catal. A: Gen. 260 (2004) 215–222.
[30] A. Dodd, A. McKinley, M. Saunders, T. Tsuzuki, Nanotechnology 17 (2006) 692–698.
[31] M. Zhang, G. Sheng, J. Fu, T. An, X. Wang, X. Hu, Mater. Lett. 59 (2005) 3641–3644.
[32] W.-W. Wang, Y.-J. Zhu, L.-X. Yang, Adv. Funct. Mater. 17 (2007) 59–64.
[33] Z. Wen, G. Wang, W. Lu, Q. Wang, Q. Zhang, J. Li, Cryst. Growth Des. 7 (2007) 1722–1725.
[34] E.M. Seftel, E. Popovici, M. Mertens, E.A. Stefaniak, R. Van Grieken, P. Cool, E.F. Vansant, Appl. Catal. B: Environ. 84 (2008) 699–705.
[35] L.R. Zheng, Y.H. Zheng, C.Q. Chen, Y.Y. Zhan, X.Y. Lin, Q. Zheng, K.M. Wei, J.F. Zhu, Inorg. Chem. 48 (2009) 1819–1825.
[36] S. Zhenya, D. Yundi, Z. Weiying, J. Nanomater. (2008), http://dx.doi.org/10.1155/2008/286069 (ID 286069).
[37] Z. Zhang, C. Shao, X. Li, L. Zhang, H. Xue, C. Wang, Y. Liu, J. Phys. Chem. C 114 (2010) 7920–7925.
[38] N. Talebian, M.R. Nilforoushan, E.B. Zargar, Appl. Surf. Sci. 258 (2011) 547–555.
[39] H. Uchiyama, R. Nagao, H. Kozuka, J. Alloys Compd. 554 (2013) 122–126.
[40] D.Y. Torres Martínez, R. Castanedo Péreza, G. Torres Delgado, O. Zelaya Ángel, J. Photochem. Photobiol. A: Chem. 235 (2012) 49–55.
[41] Z. Yang, L. Lv, Y. Dai, Z. Xv, D. Qian, Appl. Surf. Sci. 256 (2010) 2898–2902.
[42] N. Modirshahla, A. Hassani, M.A. Behnajady, R. Rahbarfam, Desalination 271 (2011) 187–192.
[43] M. Zhang, L. Li, Adv. Funct. Mater. 197-198 (2011) 1038–1041.
[44] C.-C. Lin, Y.-J. Chiang, J. Chem. Eng. 181–182 (2012) 196–205.
[45] M.T. Uddin, Y. Nicolas, C. Olivier, T. Toupance, L. Servant, M.M. Müller, H.-J. Kleebe, J. Ziegler, W. Jaegermann, Inorg. Chem 51 (2012) 7764–7773.
[46] V. Kuzhalosai, B. Subash, A. Senthilraja, P. Dhatshanamurthi, M. Shanthi, Spectrochim. Acta A 115 (2013) 876–882.
[47] A. Hamrouni, H. Lachheb, A. Houas, Mater. Sci. Eng. B 178 (2013) 1371–1379.
[48] N. Serpone, P. Maruthamuthu, P. Pichat, E. Pelizzetti, H. Hidaka, J. Photochem. Photobiol. A: Chem. 85 (1995) 247–255.
[49] M. Koizumi, Y. Yamamoto, Y. Ito, M. Takano, T. Enami, E. Kamata, R. Hasegawa, J. Toxicol. Sci. 26 (2001) 299–311.
[50] M.A. Butler, D.S. Ginley, J. Electrochem. Soc. 125 (1978) 228–232.
[51] L. Jing, Z. Xu, X. Sun, J. Shang, W. Cai, Appl. Surf. Sci. 180 (2001) 308–314.

[52] Q. Li, X. Yuan, G. Zeng, S. Xi, Mater. Chem. Phys. 47 (1997) 239–245.
[53] M.A. Butler, J. Appl. Phys. 48 (1977) 1914–1920.
[54] A.M. Roy, G.C. De, N. Sasmal, S.S. Bhattachayya, Int. J. Hydrogen Energy 20 (1995) 627–630.
[55] P. Wardman, J. Phys. Chem. Ref. Data 18 (1989) 1637–1756.
[56] K. Asokan, J.Y. Park, S.-W. Choi, S.S. Kim, Nanoscale Res. Lett. 5 (2010) 747–752.
[57] A. Di Paola, M. Bellardita, G. Marcì, L. Palmisano, F. Parrino, R. Amadelli, Catal. Today 161 (2011) 35–40.
[58] N. San, A. Hatipoglu, G. Kocturk, Z. Cinar, J. Photochem. Photobiol. A: Chem. 146 (2002) 189–197.
[59] S. Yurdakal, V. Loddo, G. Palmisano, V. Augugliaro, H. Berber, L. Palmisano, J. Adv. Oxid. Technol. 11 (2008) 501–509.
[60] T. Lopez, R. Gomez, E. Sanchez, F. Tzompantzi, L. Vera, J. Sol-Gel Sci. Technol. 22 (2001) 99–107.
[61] A. Di Paola, G. Cufalo, M. Addamo, M. Bellardita, R. Campostrini, M. Ischia, R. Ceccato, L. Palmisano, Colloids Surf. A: Physicochem. Eng. Aspects 317 (2008) 366–376.
[62] D.L. Liao, C.A. Badour, B.Q. Liao, J. Photochem. Photobiol. A 194 (2008) 11–19.
[63] S.S. Arbuj, U.P. Mulik, D.P. Amalnerkar, Nanosci. Nanotechnol. Lett. 5 (2013) 968–973.